RESEARCH   **Open Access**

Golgicide A induces pyroptosis of lung cancer stem cells by regulating dTGN formation via GOLPH3/MYO18A complex

Feng Zhang[1†], Sun-Han Zhang[1†], Teng Liu[1†], Guang-Su Xie[2†], Shi-Hua Deng[1], Ting Zhang[1], Xiao-Bian Wang[1], Yue-Yan Yang[1], Zi-Xin Chen[1], Dong-Ming Wu[1,3*] and Ying Xu[1,3*]

Abstract

Background Lung cancer is a common malignant neoplasm, one of the leading causes of death worldwide. Cancer stem cells (CSCs) drive tumor recurrence, progression, and therapeutic resistance. Thus, targeting CSCs may contribute to lung cancer treatment and improve clinical outcomes.

Methods We induced stem cell formation in serum-free suspension culture. Cell viability was assessed using the cell counting-kit 8 assay, and cell membrane integrity was evaluated using the lactate dehydrogenase release assay. Caspase-1 activity assays, western blotting, enzyme-linked immunosorbent assay, and flow cytometry were used to analyze pyroptosis in cells. Confocal microscopy was used to detect protein co-localization. Quantification of fluorescence intensity and co-localization was carried out using ImageJ software. Co-immunoprecipitation was performed to assess the interaction between GOLPH3 and MYO18A. An animal study was conducted to evaluate the effects of golgicide A (GCA) on tumor growth in vivo.

Results GCA induced cell death via pyroptosis in both H1650- and A549-derived CSCs. GCA enhanced the binding of GOLPH3 and MYO18A, resulting in trans-Golgi network (TGN) dispersion. In turn, the dispersed TGN (dTGN) recruited NLRP3. Our xenograft animal model study confirmed that GCA can inhibit tumor growth.

Conclusions GCA induced pyroptosis by promoting the interaction between GOLPH3 and MYO18A, resulting in dTGN formation in lung CSCs. Our findings provide a novel molecular insight into the anti-cancer activities of GCA in lung CSCs.

Keywords Golgicide A, Pyroptosis, Lung cancer stem cells, trans-Golgi network, GOLPH3/MYO18A

[†]Feng Zhang, Sun-Han Zhang, Teng Liu and Guang-Su Xie contributed equally to this study and are co-first authors.

*Correspondence:
Dong-Ming Wu
harvey1989@126.com
Ying Xu
yingxu825@126.com
[1]School of Clinical Medicine, The First Affiliated Hospital of Chengdu Medical College, Chengdu 610500, China
[2]Xindu District People's Hospital of Chengdu, Sichuan, PR China
[3]Clinical laboratory, the First Affiliated Hospital of Chengdu Medical College, No. 278, Baoguang Road, Chengdu, Sichuan 610500, P.R. China

Zhang *et al. Stem Cell Research & Therapy*   (2025) 16:121

Page 2 of 13

Background

Lung cancer accounts for approximately one-fifth of all cancer-related deaths worldwide. In 2020, it was the second most common cancer, with 2.21 million new cases and 1.8 million deaths [1]. Non-small-cell lung cancer (NSCLC) accounts for approximately 85% of all primary lung cancers, with lung adenocarcinoma (LUAD) being among the most common histological subtypes [2]. In LUAD patients, the major causes of death include treatment failure and metastasis, with the cancer stem cell (CSC) population considered a key driver of both [3]. CSCs comprise a small population of cells that exhibit stem cell characteristics [4, 5]. Substantial evidence indicates that CSCs can self-renew and differentiate into a variety of cell lineages, promoting tumor growth, metastasis, recurrence, and therapeutic resistance [6]. Therefore, interventions targeting lung CSCs (LCSCs) may represent an effective lung cancer treatment strategy.

Pyroptosis, a form of programmed cell death, is activated by caspases-1/4/5/11 and mediated by the inflammasome. It is distinguished by enlarging cells and blebs emerging from the plasma membrane [7–9]. It has been suggested that the pyroptosis observed in a number of diseases requires activation of the NOD-like receptor family pyrin domain-containing 3 (NLRP3) inflammasome [10–12]. When NLRP3 is activated, it oligomerizes, attaches to the adaptor protein ASC, and then recruits caspase-1 to create the NLRP3 inflammasome [13]. Subsequently, caspase-1 is activated and cleaved, which further leads to the cleavage of gasdermin D (GSDMD). This process releases the cleaved GSDMD N-terminal fragment (GSDMD-N), which induces the formation of membrane holes and encourages pyroptosis [14–16]. Moreover, activated caspase-1 promotes the production and release of pro-inflammatory cytokines, including IL-1β and IL-18 [17, 18]. In recent years, an increasing number of studies have shown a close relationship between pyroptosis and tumors [19]. More specifically, triggering pyroptosis is considered a novel approach to cancer treatment.

Through comprehensive screening analysis, we identified golgicide A (GCA) from a pyroptosis compound library (including 441 potential candidates) as a compound that could have significant anti-cancer activity against LCSCs. Previous studies have shown that GCA can effectively inhibit the replication of a wide range of viruses [20, 21]. In recent years, GCA has also been detected to restrain the growth of tumor cells [22, 23]. GCA prevents the Golgi apparatus from functioning, which may cause the Golgi and trans-Golgi network (TGN) to disintegrate [24]. To assemble the downstream adaptor complex ASC, which polymerizes in the perinuclear area before enlisting caspase-1 to initiate downstream signaling, the disintegrated TGN recruits NLRP3 [25]. Here, we investigated how GCA disintegrates the TGN to provide a fulcrum for the recruitment of NLRP3. We demonstrated that GCA exhibits potent anti-tumor effects by targeting LCSCs both in vitro and in vivo.

Methods

Cell lines and cell culture

Jenniobio Biotechnology Co., Ltd. (Guangzhou, China) provided the human lung adenocarcinoma A549 cells, and Procell Life Science & Technology Co., Ltd. (Wuhan, China) provided the H1650 cells and human normal lung epithelial BEAS-2B cells. The cell lines were cultured in DMEM supplemented with 10% fetal bovine serum (FBS) and 1% penicillin-streptomycin in an incubator set at 37 °C with 5% CO_2. The cell lines were verified by short tandem repeat (STR) DNA profile analysis.

Sphere formation assay

To conduct sphere formation experiments, A549 and H1650 cells were cultured in serum-free DMEM-F12 supplemented with 5U/l insulin, 1:1 B27, 20 ng/ml epidermal growth factor, and 20 ng/ml basic fibroblast growth factor, as previously mentioned [26]. Cells were treated for sphere culture for subsequent experiments after being incubated for six days at 37 °C with 5% CO_2 to produce first-generation spheres.

Reagents and antibodies

Anti-IL-18 and anti-GAPDH were obtained from Proteintech (Wuhan, China); anti-caspase-1, anti-GSDMD-N, anti-NLRP3, and anti-Golgi phosphoprotein-3 (GOLPH3) were obtained from Abcam (Cambridge, United Kingdom); and anti-TGN38, anti-ASC, and anti-myosin 18 A (MYO18A) were obtained from Santa Cruz Biotechnology (Dallas, United States). Beyotime Biotechnology (Shanghai, China) supplied the following secondary antibodies: FITC-labeled goat anti-mouse (A0568), Cy3-labeled goat anti-rabbit (A0516), and Cy3-labeled goat anti-mouse (A0521). GCA (S7266) and the pyroptosis compound library (L7400) were acquired from Selleck Chemicals (Houston, TX, United States).

Cell counting Kit-8 (CCK-8) assay

After seeding in 96-well plates, cells underwent the specified treatments. Cells treated with 10 μl of CCK-8 solution (Beyotime, Shanghai, China) were moved into 100 μl of new media and incubated for 1 h at 37 °C with 5% CO_2. A microplate reader was used to determine absorbance at 450 nm.

Colony-formation assays

Cells were seeded into 6-well plates (1,000 cells/well) and incubated for the entire night to create colonies. The cells were then treated with GCA, allowed to grow into cell

colonies for seven days, fixed for 10 min with 4% paraformaldehyde, and stained for 5 min with 0.5% crystal violet. ImageJ software and a light microscope were utilized to take pictures and tally the colonies.

Total RNA extraction and real-time quantitative polymerase chain reaction (RT-qPCR)

The Total RNA Extraction Kit (Solarbio, Beijing, China) was utilized to extract total RNA, and an iScript cDNA Synthesis Kit (Bio-Rad, Hercules, CA, USA) was employed for reverse transcription. RT-PCR was carried out utilizing SYBR Green (Bio-Rad) on a CFX96 Real-time System. Every step of the process was carried out as directed by the manufacturer. Ultimately, target gene mRNA expression levels were quantified relative to β-actin levels. The sequences of the primers used in this study were as follows: CD133-F, AGGCACTTACGGC ACTCTTC; CD133-R, GCTGTCATAATTCATTCTG TCTATTCC; CD44-F, TGCCGCTTTGCAGGTGTAT; CD44-R, GGCCTCCGTCCGAGAGA; nanog-F, AATAC CTCAGCCTCCAGCAGATG; nanog-R, TGCGTCACA CCATTGCTATTCTTC; sox2-F, GGACTGAGAGAAAG AAGAGGAGAGAG; sox2-R, TGCCGCCGCCGATGAT TG; oct4-F, GAGAACCGAGTGAGAGGCAACC; oct4-R, CATAGTCGCTGCTTGATCGCTTG; β-actin-F, CC TGGCACCCAGCACAAT; β-actin-R, GGGCCGGACT CGTCATAC.

Western blotting assay

Bicinchoninic acid (BCA) test kits (Beyotime, Shanghai, China) were used to measure the protein concentration after the total protein was extracted using precooled radio immunoprecipitation assay (RIPA) buffer containing protease inhibitors. Using 8–12% sodium dodecyl sulfate polyacrylamide gel electrophoresis (SDS-PAGE), the total protein was isolated and then transferred onto PVDF membranes. The primary antibodies were then incubated with the membranes for an entire night at 4 °C after the membrane had been blocked for an hour at room temperature by immersing in 5% skim milk. The secondary antibody was added and incubated at 1:8000 room temperature for 1 h, following three washes with Tris-buffered saline Tween. Binding was observed by enhanced chemiluminescence. Protein signals were assessed using Image Lab software and a ChemiDoc XRS device.

Enzyme-linked immunosorbent assay (ELISA)

Following GCA treatment, the amounts of IL-18 and IL-1β released into cell culture supernatants were measured using commercial ELISA Kits (Mlbio, Shanghai, China). The ELISA was carried out in compliance with the manufacturer's guidelines. Absorbance was measured at 450 nm. The standards included in the kit were used to generate standard curves.

Lactate dehydrogenase (LDH) release assay

At a density of 1×10^4 cells per well, logarithmic growth phase cells were seeded into 96-well plates and incubated for the entire night at 37 °C and 5% CO_2 in a cell incubator. Following the recommended course of treatment, LDH release assays were carried out in accordance with the manufacturer's instructions using the LDH Cytotoxicity Assay Kit (Beyotime, Shanghai, China).

Flow cytometry

Following the manufacturer's instructions, an Annexin V-PE/7-AAD Detection Kit (KeyGEN, Jiangsu, China) was used to measure pyroptosis via flow cytometry. After seeding the cells on 6-well plates, they were trypsinized in 0.25% trypsin without EDTA and then washed three times in phosphate-buffered saline (PBS). After that, the cells were stained for 15 min with 7-AAD. Following the reaction, 450 μl of binding buffer was added, and 1 μl of Annexin V-PE was added and incubated for 15 min at 37 °C in the dark. Lastly, a flow cytometer (FACSCalibur; Becton-Dickinson, Franklin Lakes, NJ, United States) was used to evaluate the samples.

Confocal microscopy

The cells underwent three PBS washes after being fixed for 10 min in 4% formaldehyde that had been precooled. The cells were then permeabilized using 0.02% TritonX-100, blocked for 40 min with 5% goat serum albumin, and then incubated with primary antibodies overnight at 4 °C before being incubated with the corresponding secondary antibodies. 4,6-diamidino-2-phenylindole (DAPI) was used as the mounting medium to stain the nuclei. Pictures were taken with a confocal laser-scanning microscope (Nikon, Japan).

Co-immunoprecipitation (Co-IP)

After being lysed in RIPA buffer, cells were treated with a primary antibody and gently agitated at 4 °C for the entire night. For immunoprecipitation, Protein A + G agarose (Beyotime, Shanghai, China) was utilized in accordance with the manufacturer's recommendations, and 12% SDS-PAGE was used to resolve the samples for western blotting examination.

Xenograft nude mouse model

The xenograft experiment was carried out in compliance with Chengdu Medical College's Laboratory Animal Ethics Committee requirements. We obtained female BALB/c nude mice (aged 5–6 weeks) from GemPharmatech Co. Ltd. in Chengdu, China. The animals were kept in specific pathogen-free environments at a regulated

temperature. Water for drinking, bedding, and cages were routinely replaced and autoclaved. A total of 1×10^7 cells were injected subcutaneously into the right of the dorsal midline for the xenograft tumor development assay. The nude mice were randomly assigned to three treatment groups ($n = 5$) on day 7 following tumor inoculation: a low-dose GCA group (20 mg/kg/week, dissolved in solvent), a high-dose GCA group (50 mg/kg/week, dissolved in solvent); and a control group. The treatments were administered for a duration of 4 weeks. Every four days, the weight and tumor volume of the mice were measured. The formula used to compute the tumor volume (mm^3) was volume = (length × width^2) / 2 [27]. At the end of the study, anesthesia was administered by a single intraperitoneal injection of 50 mg/kg body weight of sodium pentobarbital for at least 10 min to ensure that the mice were in a state of deep anesthesia, and then cervical dislocations were performed for humane euthanasia to minimize pain. Vicky Biotechnology (Chengdu, China) supplied the anesthetic sodium pentobarbital (WKQ-0028128). The tumor tissues were carefully removed for further investigation.

Immunohistochemical staining
The tissue slices underwent PBS washing, dehydration, and wax removal. Following antigen retrieval, the samples were boiled in citrate buffer (pH 6.0) and blocked for an hour at 37 °C using 5% normal goat serum. After an overnight incubation with the primary antibodies at 4 °C, the sections were treated with the secondary antibodies. Ultimately, the immunocomplexes were observed using diaminobenzidine (DAB) as the chromogen, and then hematoxylin counterstaining was applied.

Statistical analysis
Each in vitro test was performed at least three times independently. All animals were randomly assigned to the experimental groups. One-way analysis of variance (ANOVA) or paired t-tests were used to assess the statistical significance between the groups. GraphPad Prism 8.0 was used for all statistical analyses (GraphPad Software, USA). Statistical significance was defined as $P < 0.05$.

Results
GCA effectively suppresses the growth of LCSCs
We confirmed that LCSCs were successfully cultured by detecting the stemness gene-related markers nanog, oct4, sox2, CD44, and CD133 in spheroids prepared from A549 and H1650 cells (Supplementary Fig. 1 of Additional file 1). Utilizing single-dose primary cytotoxicity tests, we employed A549-driven CSCs to screen 441 compounds acquired from Selleck (Fig. 1A). Drugs inducing more than 60% inhibition are shown in Fig. 1B.

Next, LDH release assay and ELISA were used for subsequent screening (Fig. 1C-E). Based on the results of the above assays, we focused on GCA (structure shown in Fig. 1F) for the subsequent experiments. Figure 1G shows the dose-dependent anti-cancer effect of GCA on A549- and H1650-derived CSCs. These results were validated via colony-formation experiments using two types of LCSCs (Fig. 1H). Meanwhile, we observed that GCA had a significant suppressive effect on the viability of normal lung cancer cells, whereas it had no significant impact on normal lung epithelial cells (Supplementary Fig. 2 of Additional file 1). The results suggested that GCA has anti-cancer activity against LCSCs.

GCA induces pyroptosis of LCSCs
After 24 h of treatment with GCA, single cells dissociated from the spheroids and became inflated, resembling pyroptosis, with typical big bubbles emerging from the plasma membrane (Fig. 2A). Annexin V and PE/7-AAD double labeling was used for flow cytometry analysis because these substances can highlight pyroptotic cells as a result of membrane rupture [28]. Following GCA treatment, there was a considerable increase in the percentage of annexin V and PE/7-AAD double-positive cells (Fig. 2B). Caspase-1 activity increased significantly after treatment compared with that in the control group (Fig. 2C). Assessment of serum IL-18 and IL-1β levels yielded similar results (Fig. 2D, E). LDH release rates further confirmed the induction of pyroptosis (Fig. 2F), indicating cell membrane rupture and leakage. Western blotting was used to evaluate the levels of caspase-1 p20, IL-18, and GSDMD-N in the GCA-treated group relative to those in the control group (Fig. 2G). The cytosolic pattern-recognition receptor NLRP3 detects endogenous danger signals as well as microorganisms. When NLRP3 is activated, it combines with the adaptor protein ASC to form an inflammasome, which activates caspase-1, releases pro-inflammatory cytokines, and causes cell death [29]. NLRP3 and ASC were shown to be co-localized by confocal microscopy (Fig. 2H, I), indicating that GCA causes LCSC pyroptosis.

GCA induces disassembly of TGN and NLRP3 recruitment
Previous studies have shown that GCA markedly disrupts Golgi morphology [24]. The Golgi apparatus in vertebrate cells is made up of several stacks that have fused together to form a tight ribbon structure [30]. Transmission electron microscopy showed that Golgi bodies were dispersed in the cytoplasm following GCA treatment (Fig. 3A, B), with the non-treated group retaining flat appearance. Immunofluorescence experiments demonstrated the dramatic effects of GCA on the TGN, which caused the latter to disassemble into small vesicles that subsequently disseminated throughout the cell (Fig. 3C,
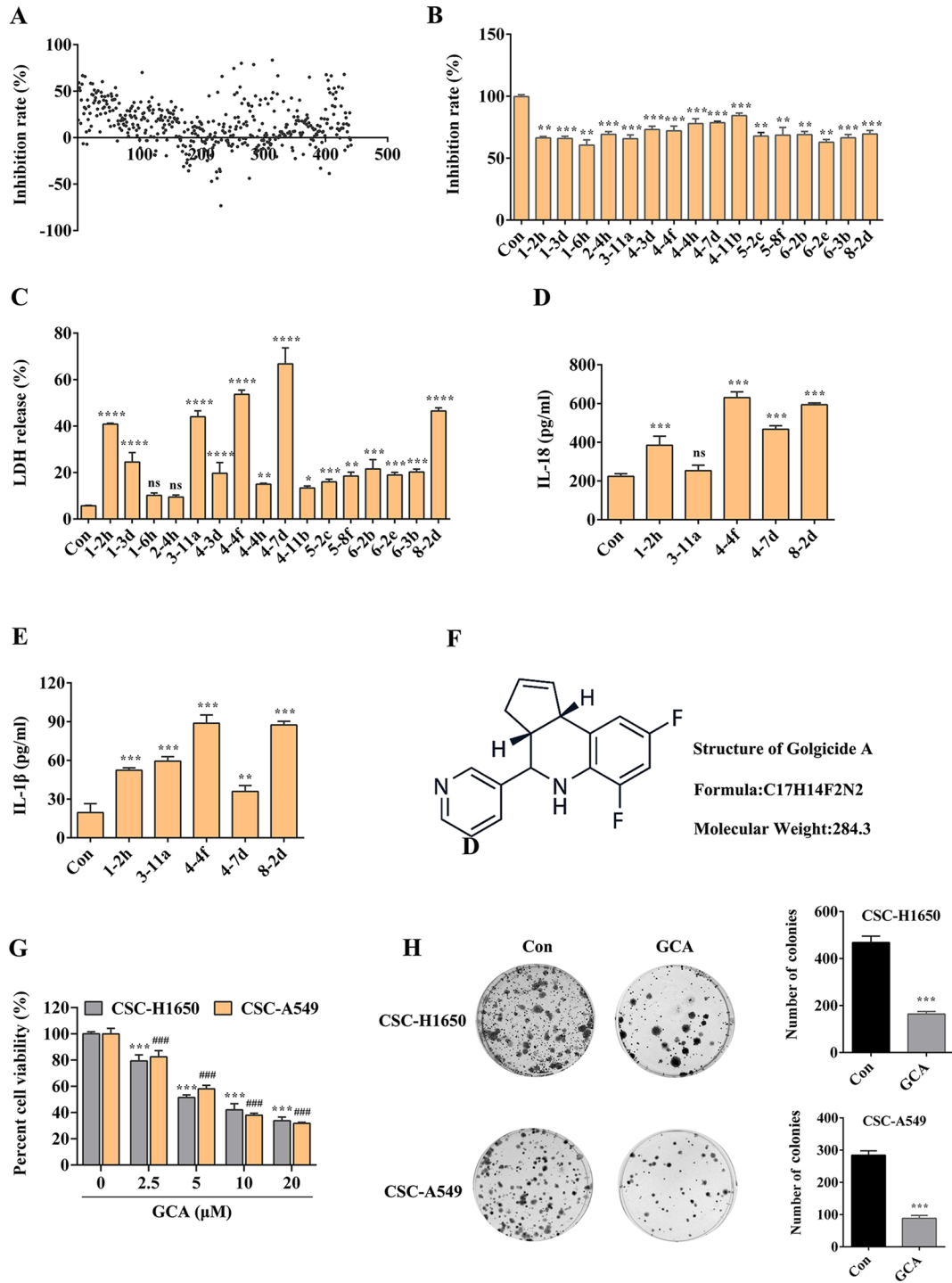
Fig. 1 Identification of GCA as a novel anti-cancer agent targeting lung cancer stem cells (LCSCs). (**A**) A549 CSCs were treated with 441 drugs for 24 h. (**B**) The top sixteen inhibitors. (**C**) Secondary screening and identification of compounds. (**D**, **E**) IL-18 and IL-1β concentration in the supernatant. (**F**) Structure of GCA. (**G**) A549 and H1650 CSCs were treated with GCA for 24 h, and cell viability was assessed. (**H**) Colony-formation assays were used to determine cell proliferation after treatment with GCA. All results were obtained from at least 3 independent experiments. Error bars represent SEM. Statistics were measured by one-way analysis of variance with Tukey's multiple comparison post hoc test with NS (non-significant) for $p > 0.05$, * for $p < 0.05$,** for $p < 0.01$,*** & ### for $p < 0.001$, **** for $p < 0.0001$
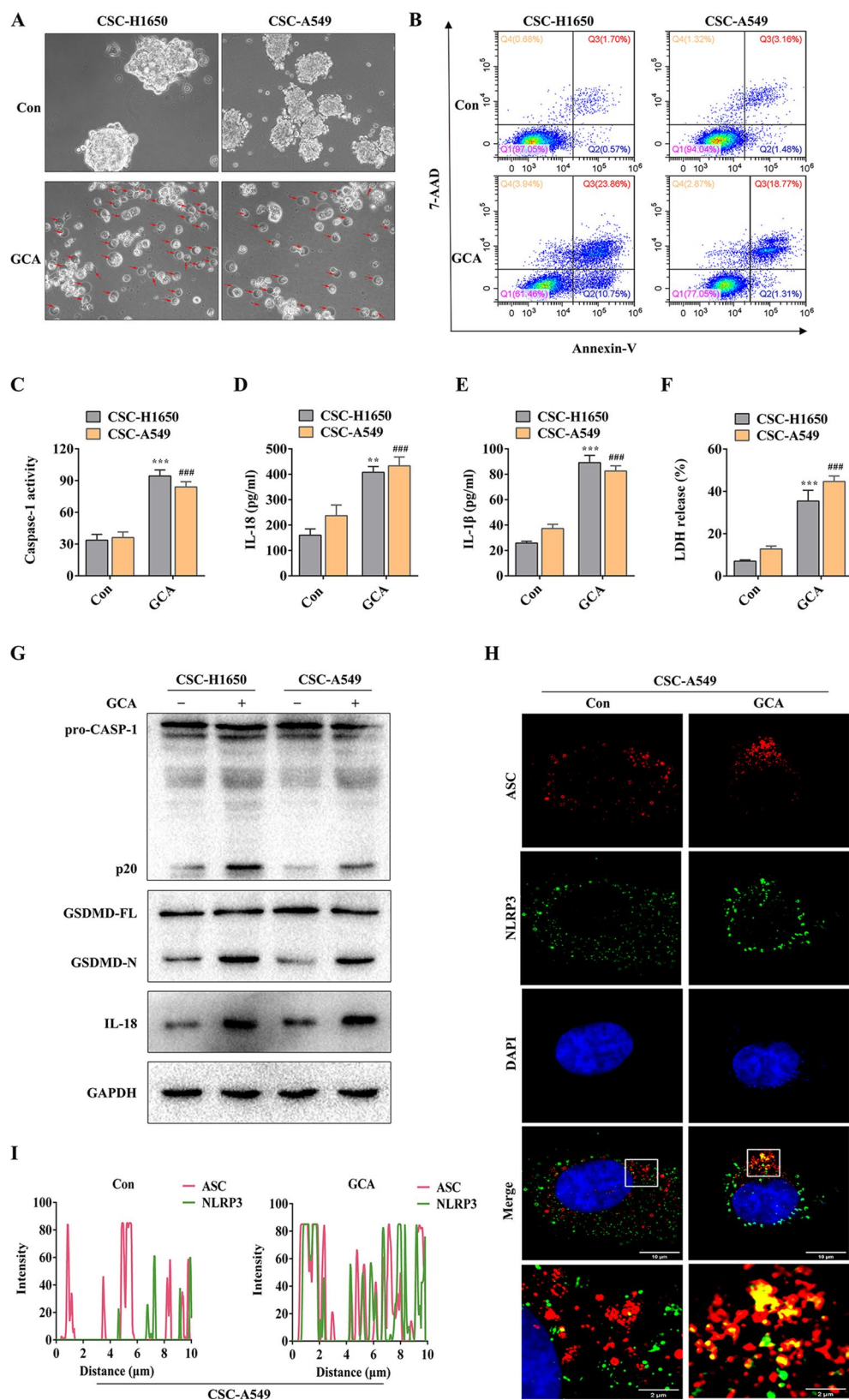
Zhang *et al. Stem Cell Research & Therapy* (2025) 16:121

Page 6 of 13

Fig. 2 (See legend on next page.)

(See figure on previous page.)

Fig. 2 GCA induces pyroptosis in lung cancer stem cells (LCSCs). (**A**) Representative images of LCSCs treated with GCA. Red arrowheads indicate the large bubbles (termed pyroptotic bodies) emerging from the plasma membrane. (**B**) The type of cell death after GCA treatment was confirmed via flow cytometry analyses using annexin V and PE/7-AAD staining. (**C**) Caspase-1 activity in LCSCs under GCA treatment. (**D**, **E**) IL-18 and IL-1β concentrations in the supernatant were determined via ELISA. (**F**) Cell death determined based on LDH release into the supernatant. (**G**) Analysis of pyroptosis markers via western blotting. (**H**) The binding between NLRP3 and ASC was detected by fluorescence co-localization. (**I**) The quantification of (**H**). All results were obtained from at least 3 independent experiments. Error bars represent SEM. Statistics were measured by one-way analysis of variance with Tukey's multiple comparison post hoc test with ** for $p < 0.01$,*** & ### for $p < 0.001$. Scale bars represent 10 μm (**H**) and 2 μm (**H**)

D). The Golgi apparatus remains a tightly organized perinuclear ribbon in untreated cells. Recent studies have shown that NLRP3 activation causes TGN disassembly, resulting in a dispersed TGN (dTGN). The dTGN provides a platform for NLRP3 oligomerization [25]. We observed that NLRP3 was recruited to the dTGN after GCA treatment (Fig. 3C-F). All these findings confirmed that GCA encourages the creation of dTGNs and the subsequent recruitment of NLRP3.

GCA enhanced the interaction of GOLPH3 with MYO18A to induce TGN dispersion

The Golgi apparatus is reportedly essential for the development of tumors and cancer [31, 32]. GOLPH3 is a component of the TGN and has a variety of functions [31, 33]. GOLPH3 binds to MYO18A and connects trans-Golgi membranes to F-actin, thus providing a tensile force required for efficient tubule and vesicle formation [34]. Next, we examined the interaction between GOLPH3 and MYO18A following GCA treatment. Our experiments confirmed that GOLPH3 localization to the Golgi apparatus was unchanged following GCA treatment (Fig. 4A, B). To explore the binding mode of GOLPH3 to MYO18A, a docking simulation study was performed by computationally predicting the possible binding sites on the surface of the protein molecule (Fig. 4C). According to the data, there were hydrogen-bonding interactions between GCA and GOLPH3 residues M199 and T200, as well as π-CH interactions involving M199, suggesting that GCA has a direct effect on the structural conformation of GOLPH3. Additionally, the docking score between GCA and the MYO18A/GOLPH3 complex was −6.11 Kcal/mol. GCA treatment enhanced the interaction between GOLPH3 and MYO18A (Fig. 4D-F). Our experiments confirmed that the effects of GCA on cell morphology did not result from actin cytoskeleton disruption (Fig. 4G). Further, we showed that GCA enhances the binding of GOLPH3 to MYO18A, resulting in TGN dispersion.

GCA inhibits tumor growth in xenograft animal models

To determine whether GCA suppressed tumor growth in vivo, A549-derived CSCs were subcutaneously injected into the right side of the dorsal midline in mice. Three treatment groups of xenograft mice were formed starting on the seventh day post-tumor implantation, as illustrated in Fig. 5A, B. The excised tumors are shown in

Fig. 5C. In comparison to that in the PBS-negative control group, the tumor growth rate was significantly suppressed in the treatment groups (Fig. 5D). Consistently, tumor weight in mice of the GCA treatment group was significantly lower than that of mice in the PBS treatment group (Fig. 5E). Our data clearly indicate that GCA inhibited the growth of LCSCs in vivo.

GCA suppressed tumor growth in xenograft mice through pyroptosis induction

We subjected tumor tissues to hematoxylin and eosin staining to evaluate pathological changes (Fig. 6A). Immunohistochemistry was used to further assess the effect of GCA on tumor tissues. The results showed that the GCA-treated group had higher expression of IL-18 and IL-1β than the control (PBS) group (Fig. 6B), which is in line with the in vitro experiment results. Western blotting confirmed that GCA inhibited tumor growth through the induction of pyroptosis in vivo (Fig. 6C).

Discussion

Over the last few decades, various new therapeutic strategies have been developed to combat cancer, such as nanomedicines [35], targeted therapy [36], and immunotherapy [37]. However, cancer remains a major cause of mortality in developed and developing countries worldwide. Resistance to chemotherapeutic agents represents a major challenge in the battle against cancer, with CSCs being the main driver of such resistance [4]. CSCs are less sensitive to classical anti-cancer agents inducing apoptosis [38]. In recent years, the significance of pyroptosis in cancer has received considerable attention. However, research on pyroptosis and related drugs targeting LCSCs remains limited. In this study, GCA, an FDA-approved small-molecule drug, exhibited cytotoxicity against LCSCs.

We screened 441 small-molecule compounds in A549-derived CSCs. Drugs with inhibition rates greater than 60% were subjected to subsequent screening, which showed that GCA had the greatest pyroptosis-inducing effect. Thus, we explored its effect on cell viability and Golgi morphology in H1650- and A549-derived CSCs. ELISA, western blotting, and flow cytometry confirmed that GCA could induce inflammatory reactions and the production of pro-inflammatory cytokines, including IL-1 β and IL-18. Moreover, a xenograft mouse model demonstrated the anti-tumor properties of GCA. These
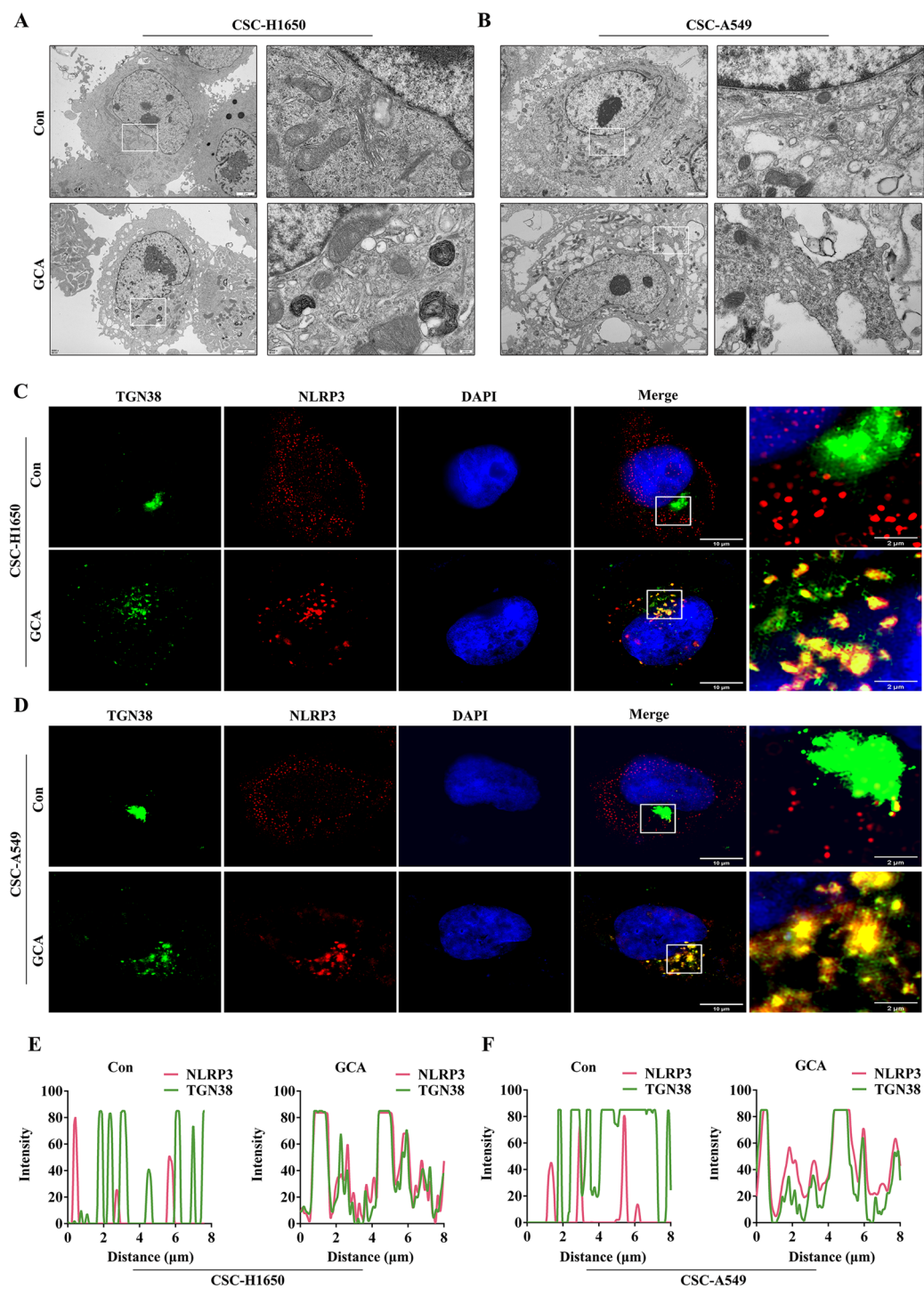
Fig. 3 NLRP3 aggregates on dTGN. (**A**, **B**) The features of pyroptosis in H1650- and A549-derived CSCs were observed via transmission electron microscopy. (**C**, **D**) LCSCs were stained for TGN38 (green), NLRP3 (red), and analyzed via confocal microscopy. (**E**, **F**) Fluorescence quantitative analysis of two kinds of LCSCs. All results were obtained from at least 3 independent experiments. Scale bars represent 200 μm (**A** and **B**), 10 μm (**C** and **D**), and 2 μm (**A**, **B**, **C** and **D**)
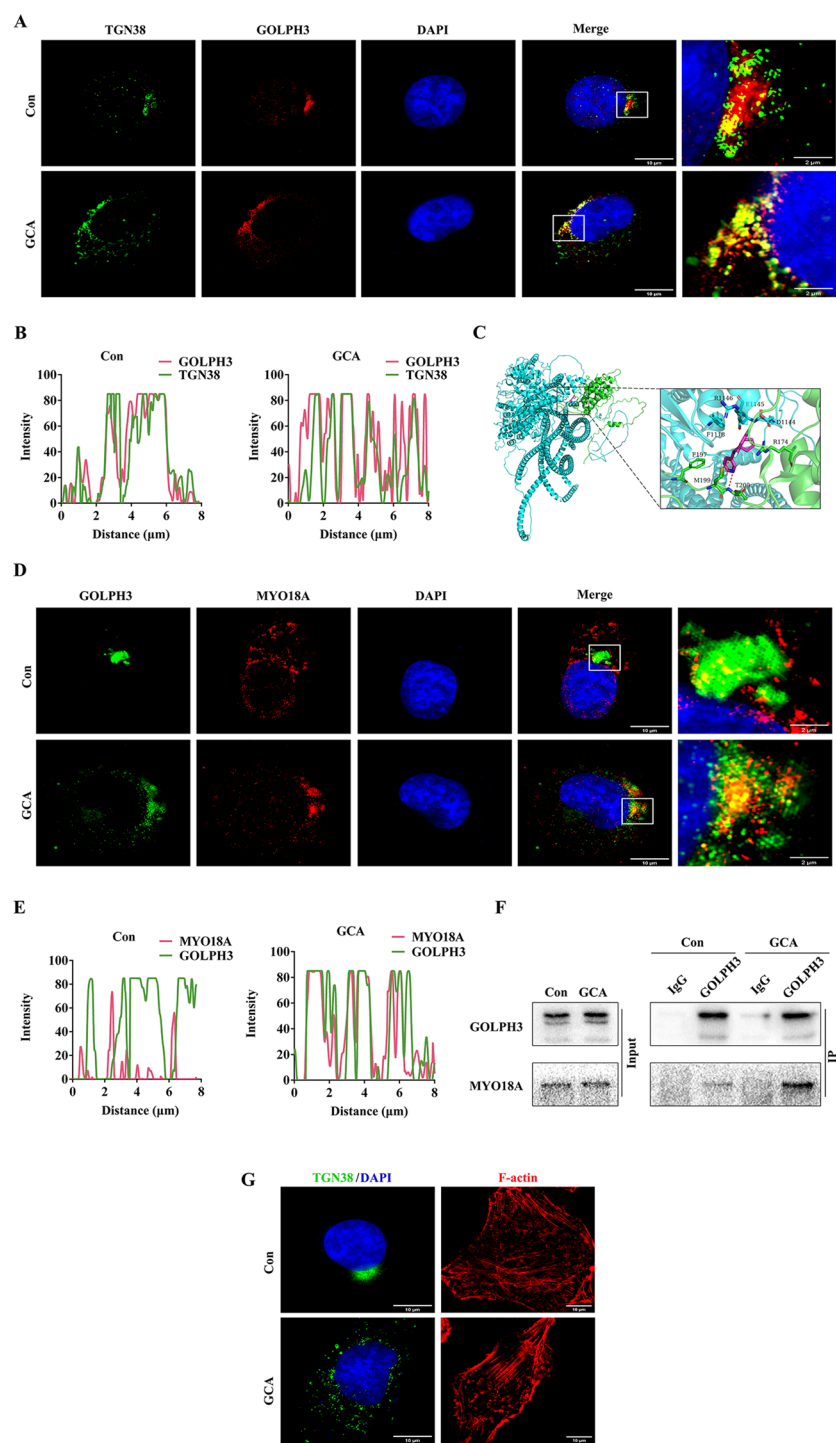
Fig. 4 GCA enhanced the interaction between GOLPH3 and MYO18A. (**A**) A549-derived CSCs were stained for TGN38 (green) and GOLPH3 (red) and analyzed via confocal microscopy. (**B**) The quantification of (**A**). (**C**) The 3D binding model of GCA and GOLPH3/MYO18A complex. GOLPH3 is colored green, the residues in GOLPH3 are shown as green sticks, MYO18A is colored cyan, the residues in MYO18A are shown as cyan sticks, and GCA is shown as a magenta stick. The red dashes represent hydrogen bond interactions. The orange dashes represent π-CH interaction. (**D**) The interaction of GOLPH3 with MYO18A after GCA treatment was detected via confocal microscopy. (**E**) The quantification of (**D**). (**F**) Co-IP analysis of the interaction between MYO18A and GOLPH3 in A549-derived CSCs after treatment with GCA. (**F**) GCA had no effects on actin microfilaments. All results were obtained from at least 3 independent experiments. Scale bars represent 10 μm (**A**, **D** and **E**) and 2 μm (**A** and D)
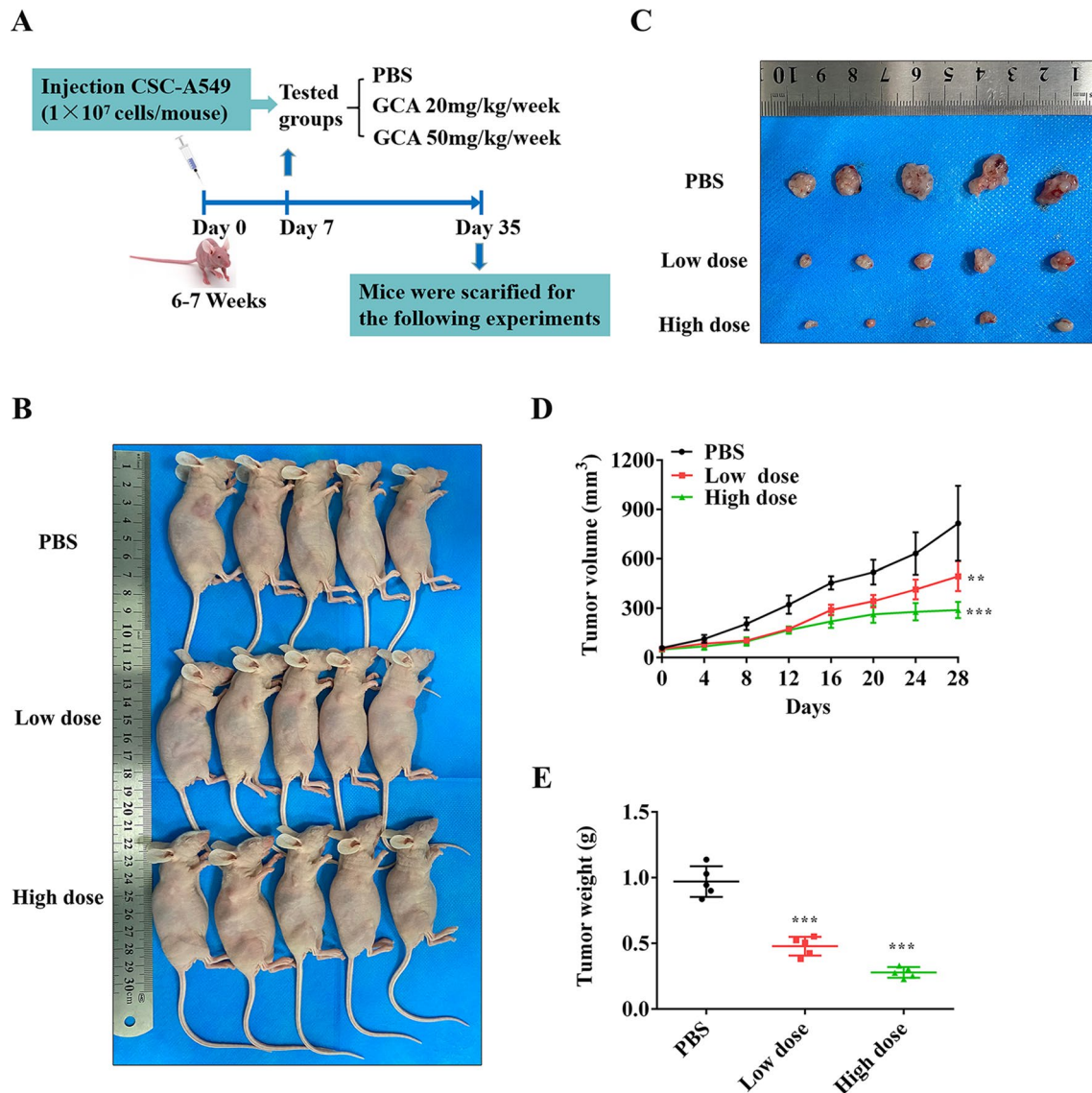
Fig. 5 Anti-tumor effect of GCA in xenograft models injected with lung cancer stem cells (LCSCs). (**A**) The experimental design for GCA treatment in vivo. (**B**) Images of nude mice with subcutaneous xenografts in the indicated groups. (**C**) Representative images of tumors taken at the end of the study. (**D**) Tumor growth curves of established LCSC xenografts in nude mice during therapy under different treatments. (**E**) Tumor weight in the three treatment groups. All results were obtained from at least 3 independent experiments. Error bars represent SEM. Statistics were measured by one-way analysis of variance with Tukey's multiple comparison post hoc test with ** for $p < 0.01$,*** for $p < 0.001$

results were in line with earlier research demonstrating the anti-tumor effect of GCA in lung and breast cancer cells [22, 23].

On the cytoplasmic side of the Golgi membrane, peripheral Golgi proteins interact with actin networks and microtubules to control Golgi morphology. Changes in Golgi morphology are related to the regulation of various processes, including directed migration [32], stress [39], DNA repair [40], mitosis [41], pro-inflammatory responses [25], and autophagy [42]. The Golgi architecture is centered on a compact ribbon structure. The absence of the Golgi ribbon is linked to a number of illnesses and conditions. Its fragmentation is implicated

in neurodegenerative diseases [43] and cancer [44]. The small molecule drug GCA inhibits protein trafficking and causes disintegration of the Golgi apparatus. Our study found that dTGN provided a platform for the oligomerization of NLRP3 and subsequent assembly of the downstream adaptor complex ASC.

An increasing body of evidence highlights the importance of organelle-dependent cell death. In this study, we demonstrated that GOLPH3, a highly conserved protein, is concentrated in the TGN. GOLPH3 is upregulated in various human solid tumors and is involved in tumor progression [45]. GOLPH3 promotes cell proliferation by enhancing growth factor-induced mammalian target
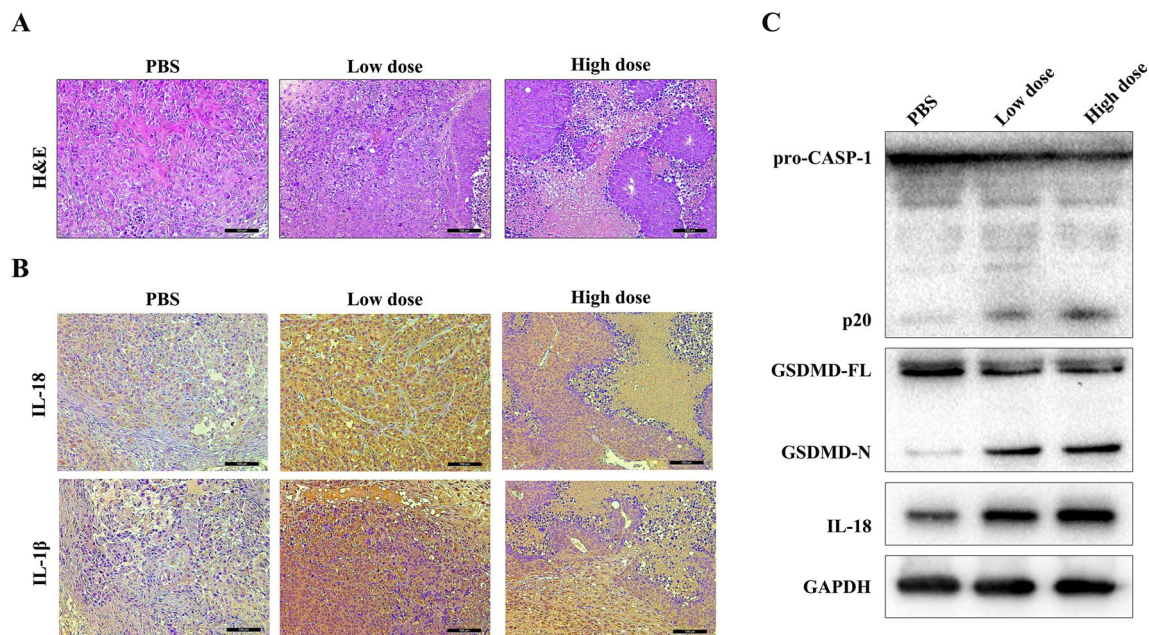
Fig. 6 GCA induced lung cancer stem cell (LCSC) pyroptosis in vivo. **(A)** Hematoxylin and eosin staining of drug-treated subcutaneous tumors. **(B)** Immunohistochemistry staining of IL-18 and IL-1β in inhibitor-treated tumors in nude mice. **(C)** The protein levels of caspase-1 p20, GSDMD-N, and IL-18 in tumor tissues were detected via western blotting. GAPDH was included as a loading control. All results were obtained from at least 3 independent experiments. Scale bars represent 100 μm (**A** and **B**)

of rapamycin (mTOR) signaling and alters the response of cancer cells to rapamycin, an mTOR inhibitor, in vivo [46]. Additionally, GOLPH3 binds to MYO18A and connects trans-Golgi membranes. Through co-IP and immunofluorescence experiments, we proved that the binding between GOLPH3 and MYO18A was enhanced after GCA treatment, which was essential for dTGN formation.

Conclusions

In summary, the findings of this investigation highlighted GCA as a promising anti-cancer agent targeting LCSCs. GCA exerted its anti-tumor effects through the induction of pyroptosis. The main mechanism of action involves dTGN formation through the enhanced binding between GOLPH3 and MYO18A. After NLRP3 is recruited, the activated inflammasome cleaves GSDMD, releases inflammatory factors, and promotes the inflammatory cascade. Taken together, these results point to GCA as a possible medication for LCSC targeting.

Abbreviations
CSC	Cancer stem cell
NSCLC	Non-small-cell lung cancer
LUAD	Lung adenocarcinoma
LCSC	Lung cancer stem cell
NLRP3	NOD-like receptor family pyrin domain-containing 3
GSDMD-N	GSDMD N-terminal fragment
GCA	Golgicide A
TGN	Trans-Golgi network
CCK-8	Cell counting kit-8
RIPA	Radioimmunoprecipitation assay
PBS	Phosphate-buffered saline
FBS	Fetal bovine serum
SDS-PAGE	Sodium dodecyl sulfate polyacrylamide gel electrophoresis
ELISA	Enzyme-linked immunosorbent assay
LDH	Lactate dehydrogenase
Co-IP	Co-immunoprecipitation
RT-PCR	Real-time quantitative polymerase chain reaction
dTGN	Dispersed TGN

Supplementary Information

The online version contains supplementary material available at https://doi.or g/10.1186/s13287-025-04246-0.

Supplementary Fig. 1: Culture and identification of lung cancer stem cells. (A) Spheroids prepared from H1650 and A549 cells. (B) The expression of stemness markers in H1650 and A549 spheroids cells and corresponding parental cells was detected by qRT-PCR. Error bars represent SEM. Statistics were measured by one-way analysis of variance with Tukey's multiple comparison post hoc test with NS (non-significant) for p > 0.05, * for p < 0.05,** for p < 0.01,*** for p < 0.001, **** for p < 0.0001

Supplementary Fig. 2: The role of GCA for other cell lines. (A) Colony-formation assays revealed the effect of GCA on the proliferative capacity of cells from different cell lines. (B) Cell viability was assessed in different groups by CCK-8 assay. Error bars represent SEM. Statistics were measured by one-way analysis of variance with Tukey's multiple comparison post hoc test with NS (non-significant) for p > 0.05, *** for p < 0.001

Supplementary Material 3

Supplementary Material 4

Supplementary Material 5

Zhang *et al. Stem Cell Research & Therapy*   (2025) 16:121

Page 12 of 13

Data availability
Data supporting the findings of this study are available from the corresponding author upon request.

Declarations

Ethics approval and consent to participate
The animal study protocol was reviewed and approved by the Animal Policy and Welfare Committee of Chengdu Medical College (CMC-IACUC-2021024; Title: Precision Intervention Strategies for Multiple Diseases with Novel Programmed Cell Death as a Pathogenetic Mechanism; Date of approval: December 31, 2021). The manuscript adhered to the ARRIVE guidelines for the reporting of animal experiments. All animal experiments were carefully performed to avoid animal suffering. The human-derived BEAS-2B has been commercialized and is available for legal purchase under Patent US4885238.

Consent for publication
Not applicable.

Competing interests
The authors have declared that no competing interest exists.

References
1. Sung H, Ferlay J, Siegel RL, Laversanne M, Soerjomataram I, Jemal A, et al. Global cancer statistics 2020: GLOBOCAN estimates of incidence and mortality worldwide for 36 cancers in 185 countries. CA Cancer J Clin. 2021;71:209–49. https://doi.org/10.3322/caac.21660.
2. Midha A, Dearden S, McCormack R. EGFR mutation incidence in non-small-cell lung cancer of adenocarcinoma histology: a systematic review and global map by ethnicity (mutMapII). Am J Cancer Res. 2015;5:2892–911.
3. Maiuthed A, Chantarawong W, Chanvorachote P. Lung cancer stem cells and cancer stem cell-targeting natural compounds. Anticancer Res. 2018;38:3797–809. https://doi.org/10.21873/anticanres.12663.
4. Koren E, Fuchs Y. The bad seed: cancer stem cells in tumor development and resistance. Drug Resist Updat. 2016;28:1–12. https://doi.org/10.1016/j.drup.2016.06.006.
5. Adorno-Cruz V, Kibria G, Liu X, Doherty M, Junk DJ, Guan D, et al. Cancer stem cells: targeting the roots of cancer, seeds of metastasis, and sources of therapy resistance. Cancer Res. 2015;75:924–9. https://doi.org/10.1158/0008-5472.CAN-14-3225.
6. O'Brien CA, Kreso A, Jamieson CH. Cancer stem cells and self-renewal. Clin Cancer Res. 2010;16:3113–20. https://doi.org/10.1158/1078-0432.CCR-09-2824.
7. Bergsbaken T, Fink SL, Cookson BT. Pyroptosis: host cell death and inflammation. Nat Rev Microbiol. 2009;7:99–109. https://doi.org/10.1038/nrmicro2070.
8. Yang JR, Yao FH, Zhang JG, Ji ZY, Li KL, Zhan J, et al. Ischemia-reperfusion induces renal tubule pyroptosis via the CHOP-caspase-11 pathway. Am J Physiol Ren Physiol. 2014;306:F75–84. https://doi.org/10.1152/ajprenal.00117.2013.
9. Galluzzi L, Vitale I, Aaronson SA, Abrams JM, Adam D, Agostinis P, et al. Molecular mechanisms of cell death: recommendations of the nomenclature committee on cell death 2018. Cell Death Differ. 2018;25:486–541. https://doi.org/10.1038/s41418-017-0012-4.
10. Wang S, Yuan YH, Chen NH, Wang HB. The mechanisms of NLRP3 inflammasome/pyroptosis activation and their role in Parkinson's disease. Int Immunopharmacol. 2019;67:458–64. https://doi.org/10.1016/j.intimp.2018.12.019.
11. Wu X, Zhang H, Qi W, Zhang Y, Li J, Li Z, et al. Nicotine promotes atherosclerosis via ROS-NLRP3-mediated endothelial cell pyroptosis. Cell Death Dis. 2018;9:171. https://doi.org/10.1038/s41419-017-0257-3.
12. Chen X, Liu G, Yuan Y, Wu G, Wang S, Yuan L. NEK7 interacts with NLRP3 to modulate the pyroptosis in inflammatory bowel disease via NF-κB signaling. Cell Death Dis. 2019;10:906. https://doi.org/10.1038/s41419-019-2157-1.
13. Lamkanfi M, Dixit VM. Mechanisms and functions of inflammasomes. Cell. 2014;157:1013–22. https://doi.org/10.1016/j.cell.2014.04.007.
14. Shi J, Zhao Y, Wang K, Shi X, Wang Y, Huang H, et al. Cleavage of GSDMD by inflammatory caspases determines pyroptotic cell death. Nature. 2015;526:660–5. https://doi.org/10.1038/nature15514.
15. Russo HM, Rathkey J, Boyd-Tressler A, Katsnelson MA, Abbott DW, Dubyak GR. Active caspase-1 induces plasma membrane pores that precede pyroptotic Lysis and are blocked by lanthanides. J Immunol. 2016;197:1353–67. https://doi.org/10.4049/jimmunol.1600699.
16. Sborgi L, Rühl S, Mulvihill E, Pipercevic J, Heilig R, Stahlberg H, et al. GSDMD membrane pore formation constitutes the mechanism of pyroptotic cell death. EMBO J. 2016;35:1766–78. https://doi.org/10.15252/embj.201694696.
17. Man SM, Kanneganti TD. Converging roles of caspases in inflammasome activation, cell death and innate immunity. Nat Rev Immunol. 2016;16:7–21. https://doi.org/10.1038/nri.2015.7.
18. He WT, Wan H, Hu L, Chen P, Wang X, Huang Z, et al. Gasdermin D is an executor of pyroptosis and required for interleukin-1beta secretion. Cell Res. 2015;25:1285–98. https://doi.org/10.1038/cr.2015.139.
19. Fang Y, Tian S, Pan Y, Li W, Wang Q, Tang Y, et al. Pyroptosis: A new frontier in cancer. Biomed Pharmacother. 2020;121:109595. https://doi.org/10.1016/j.biopha.2019.109595.
20. van der Linden L, van der Schaar HM, Lanke KH, Neyts J, van Kuppeveld FJ. Differential effects of the putative GBF1 inhibitors golgicide A and AG1478 on enterovirus replication. J Virol. 2010;84:7535–42. https://doi.org/10.1128/JVI.02684-09.
21. Martínez JL, Arnoldi F, Schraner EM, Eichwald C, Silva-Ayala D, Lee E, et al. The guanine nucleotide exchange factor GBF1 participates in rotavirus replication. J Virol. 2019;93. https://doi.org/10.1128/JVI.01062-19.
22. Ramírez-Peinado S, Ignashkova TI, van Raam BJ, Baumann J, Sennott EL, Gendarme M, et al. TRAPPC13 modulates autophagy and the response to golgi stress. J Cell Sci. 2017;130:2251–65. https://doi.org/10.1242/jcs.199521.
23. Luchsinger C, Aguilar M, Burgos PV, Ehrenfeld P, Mardones GA. Functional disruption of the golgi apparatus protein ARF1 sensitizes MDA-MB-231 breast cancer cells to the antitumor drugs actinomycin D and vinblastine through ERK and AKT signaling. PLoS ONE. 2018;13:e0195401. https://doi.org/10.1371/journal.pone.0195401.
24. Sáenz JB, Sun WJ, Chang JW, Li J, Bursulaya B, Gray NS, et al. Golgicide A reveals essential roles for GBF1 in golgi assembly and function. Nat Chem Biol. 2009;5:157–65. https://doi.org/10.1038/nchembio.144.
25. Chen J, Chen ZJ. PtdIns4P on dispersed trans-Golgi network mediates NLRP3 inflammasome activation. Nature. 2018;564:71–6. https://doi.org/10.1038/s41586-018-0761-3.
26. Zhang X, Lou Y, Zheng X, Wang H, Sun J, Dong Q, et al. Wnt blockers inhibit the proliferation of lung cancer stem cells. Drug Des Devel Ther. 2015;9:2399–407. https://doi.org/10.2147/DDDT.S76602.
27. Yan H, Luo B, Wu X, Guan F, Yu X, Zhao L, et al. Cisplatin induces pyroptosis via activation of MEG3/NLRP3/caspase-1/GSDMD pathway in triple-negative breast cancer. Int J Biol Sci. 2021;17:2606–21. https://doi.org/10.7150/ijbs.60292.
28. Wang Y, Gao W, Shi X, Ding J, Liu W, He H, et al. Chemotherapy drugs induce pyroptosis through caspase-3 cleavage of a gasdermin. Nature. 2017;547:99–103. https://doi.org/10.1038/nature22393.
29. Stutz A, Kolbe CC, Stahl R, Horvath GL, Franklin BS, van Ray O, et al. NLRP3 inflammasome assembly is regulated by phosphorylation of the Pyrin domain. J Exp Med. 2017;214:1725–36. https://doi.org/10.1084/jem.20160933.
30. Makhoul C, Gosavi P, Gleeson PA. The golgi architecture and cell sensing. Biochem Soc Trans. 2018;46:1063–72. https://doi.org/10.1042/BST20180323.

31. Kuna RS, Field SJ. GOLPH3: a golgi phosphatidylinositol(4)phosphate effector that directs vesicle trafficking and drives cancer. J Lipid Res. 2019;60:269–75. https://doi.org/10.1194/jlr.R088328.
32. Millarte V, Farhan H. The golgi in cell migration: regulation by signal transduction and its implications for cancer cell metastasis. Sci World J. 2012;2012:498278. https://doi.org/10.1100/2012/498278.
33. Zhou X, Xue P, Yang M, Shi H, Lu D, Wang Z, et al. Protein kinase D2 promotes the proliferation of glioma cells by regulating golgi phosphoprotein 3. Cancer Lett. 2014;355:121–9. https://doi.org/10.1016/j.canlet.2014.09.008.
34. Dippold HC, Ng MM, Farber-Katz SE, Lee SK, Kerr ML, Peterman MC, et al. GOLPH3 bridges phosphatidylinositol-4- phosphate and actomyosin to stretch and shape the golgi to promote budding. Cell. 2009;139:337–51. https://doi.org/10.1016/j.cell.2009.07.052.
35. Tran S, DeGiovanni PJ, Piel B, Rai P. Cancer nanomedicine: a review of recent success in drug delivery. Clin Transl Med. 2017;6:44. https://doi.org/10.1186/s40169-017-0175-0.
36. Somaiah N, Simon GR. Molecular targeted therapy in non-small cell lung cancer: an overview of available agents. J Thorac Oncol. 2009;4(11):S1046–56. https://doi.org/10.1097/01.JTO.0000361747.56424.f7.
37. Zhang H, Chen J. Current status and future directions of cancer immuno-therapy. J Cancer. 2018;9:1773–81. https://doi.org/10.7150/jca.24577.
38. Rivera C, Rivera S, Loriot Y, Vozenin MC, Deutsch E. Lung cancer stem cell: new insights on experimental models and preclinical data. J Oncol. 2011;2011:549181. https://doi.org/10.1155/2011/549181.
39. Sasaki K, Yoshida H. Organelle autoregulation-stress responses in the ER, golgi, mitochondria and lysosome. J Biochem. 2015;157:185–95. https://doi.org/10.1093/jb/mvv010.
40. Farber-Katz SE, Dippold HC, Buschman MD, Peterman MC, Xing M, Noakes CJ, et al. DNA damage triggers golgi dispersal via DNA-PK and GOLPH3. Cell. 2014;156:413–27. https://doi.org/10.1016/j.cell.2013.12.023.
41. Rabouille C, Kondylis V. Golgi ribbon unlinking: an organelle-based G2/M checkpoint. Cell Cycle. 2007;6:2723–9. https://doi.org/10.4161/cc.6.22.4896.
42. Lamb CA, Yoshimori T, Tooze SA. The autophagosome: origins unknown, biogenesis complex. Nat Rev Mol Cell Biol. 2013;14:759–74. https://doi.org/10.1038/nrm3696.
43. Liu CY, Mei M, Li Q, Roboti P, Pang Q, Ying Z, et al. Loss of the golgin GM130 causes golgi disruption, purkinje neuron loss, and ataxia in mice. Proc Natl Acad Sci U S A. 2017;114:346–51. https://doi.org/10.1073/pnas.1608576114.
44. McKinnon CM, Mellor H. The tumor suppressor RhoBTB1 controls golgi integrity and breast cancer cell invasion through METTL7B. BMC Cancer. 2017;17:145. https://doi.org/10.1186/s12885-017-3138-3.
45. Arriagada C, Cavieres VA, Luchsinger C, González AE, Muñoz VC, Cancino J, et al. GOLPH3 regulates EGFR in T98G glioblastoma cells by modulating its glycosylation and ubiquitylation. Int J Mol Sci. 2020;21. https://doi.org/10.3390/ijms21228880.
46. Scott KL, Kabbarah O, Liang MC, Ivanova E, Anagnostou V, Wu J, et al. GOLPH3 modulates mTOR signalling and Rapamycin sensitivity in cancer. Nature. 2009;459:1085–90. https://doi.org/10.1038/nature08109.

Publisher's note

Springer Nature remains neutral with regard to jurisdictional claims in published maps and institutional affiliations.